Unique composition and evolutionary histories of low velocity mantle domains

This manuscript is a non-peer reviewed preprint submitted to EarthArXiv. The manuscript has been submitted for peer review in Nature Communications.

James Panton[1*], J. Huw Davies[1], Paula Koelemeijer[2], Jeroen Ritsema[3], Robert Myhill[4]

[1*]School of Earth and Environmental Sciences, Cardiff University, Park Place, Cardiff, CF10 3AT, Wales, UK.
[2]Department of Earth Sciences, University of Oxford, South Parks Road, Oxford, OX1 3AN, England, UK.
[3]Department of Earth and Environmental Sciences, University of Michigan, 1100 North University Avenue, Ann Arbor, 40819, MI, USA.
[4]School of Earth Sciences, University of Bristol, Queens Road, Bristol, BS8 1RJ, England, UK.

*Corresponding author(s). E-mail(s): pantonjc@cardiff.ac.uk;

Abstract

The two "large low velocity provinces" (LLVPs) are broad seismic wave speed anomalies in Earth's lower mantle beneath Africa and the Pacific Ocean. Recent research suggests they represent volumes that contain relatively dense subducted oceanic crust (SOC), but the distribution of recycled material within them is an open question. Using simulations of 3-D global-scale mantle circulation over the past 1 Gyr, we find that simulated large low velocity provinces (S-LLVPs), with similar properties and locations to LLVPs, develop as a consequence of the recycling of SOC. The Pacific S-LLVP is enriched in SOC by up to 53% compared to the African S-LLVP and is therefore more dense, potentially explaining topological differences between the two structures. Shear wave velocity reductions in the two domains are similar due to the dominating influence of temperature over composition. Differences in melting ages between the two S-LLVPs reveal distinct

formation histories, where the Pacific S-LLVP is maintained by a steady replenishment of young SOC, while the African S-LLVP comprises older, well mixed material.

1 Introduction

The large low velocity provinces (LLVPs) in the lower mantle are robustly determined low seismic wave speed anomalies identified in tomographic maps of Earth's mantle [1]. Their composition, formation, and longevity have been the focus of many geodynamic and seismological investigations [1–3]. These have led to an understanding that the LLVPs represent anomalously hot regions [4] that may have a high proportion of dense subducted oceanic crust (SOC) [5, 6], iron-rich, primitive crust [7] or primordial material [8, 9].

Previous 3-D mantle circulation studies show that the historical polarity and orientations of subduction zones determine the formation histories and present-day geometries of LLVPs [10–12]. In the context of LLVPs of a primordial origin, subducting slabs sweep a layer of anomalously dense material into distinct piles beneath the Pacific and Africa [10, 12, 13]. While there have been numerous studies into the formation of LLVPs from a dense primordial layer [e.g. 10, 11, 14], studies of the contribution of SOC to LLVP formation have largely been limited to 2D geometry [5, 15–17]. These have been useful to explore the factors affecting pile formation [5, 15, 18] and have identified the ratio of intrinsic to thermal buoyancy contributions (i.e. the buoyancy number) as a key parameter in determining the rate of segregation of SOC to the lowermost mantle. However, a 3-D approach is necessary to investigate the shape, location and evolution of the LLVPs within Earth's mantle.

While the wave speed reductions in the African and Pacific LLVPs are similar, the two regions differ topologically, with the African LLVP reaching up to 550km higher above the CMB than its counterpart [19, 20]. Some researchers argue that the topological differences are due to different compositions [21], which would imply that the LLVPs have distinct formation histories. Geochemical evidence from an analysis of plume lavas associated with the two regions [22] appears to support this theory. However, others suggest that apparent geochemical differences are due to sampling bias and argue that there is no significant difference between the isotopic composition of plumes originating from the African and Pacific LLVPs [23], with topological differences due to limited seismic resolution [24, 25]. In addition, recent studies suggest that within each LLVP there may be spatial variations in geochemistry [26] as well as depth variations in composition [7].

A lack of geodynamic studies into the formation of LLVPs from SOC in 3-D geometry means we do not know whether LLVPs can dynamically form this way and whether they would form simultaneously or independently. To address this, we use the 3D mantle circulation code TERRA [27–29] to simulate the production and recycling of chemical heterogeneity in a plate-tectonic regime for one billion years (see Methods

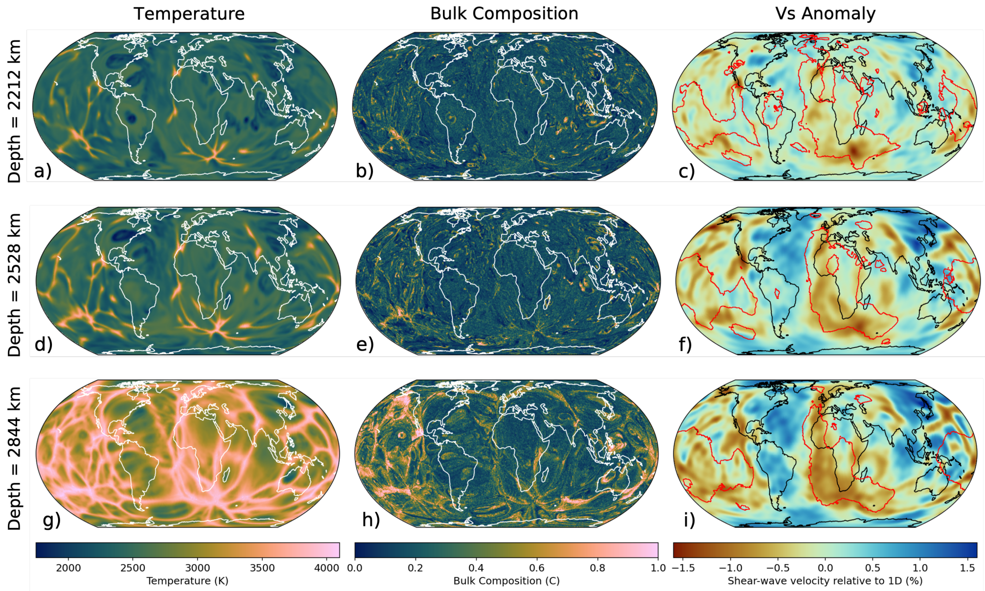

Fig. 1 Mantle structure predicted by simulation RCY showing temperature (a, d, g), bulk composition (b, e, h), and converted shear-wave speed filtered using the resolution of seismic tomography model S40RTS [35] (c, f, i) at 2212 km (top tow), 2528 km (middle row) and 2845 km (bottom row) depth. Red lines plotted on top of shear wave velocity maps outline the margins of the LLVPs in a "vote map" of 18 shear wave tomography models [36], indicating where at least 5 models are in agreement.

6.1). This long model duration is important for replenishing pile material after entrainment [15, 30]. Kinematic reconstructions of plate motions [31] are used to constrain surface plate velocities and the paleo-locations of subduction zones and spreading ridges. The simulations include generation of oceanic crust by melting at mid-ocean ridges and plume heads [32–34] and its recycling into the mantle (see Methods 6.2).

2 Simulated shear wave velocity anomalies

Previous work by Panton et al. [30] shows that for buoyancy numbers in the range of 0.55 – 0.66, SOC segregated to the lowermost mantle is in a quasi-steady state – it is not immediately entrained, but it also remains mobile enough that it does not completely blanket the CMB. Assuming a coefficient of thermal expansion of $\sim 1.2 \times 10^5 K^1$ [37] at the base of the mantle, a buoyancy number (see Methods 6.1) of 0.66 corresponds to an excess density of +2.1% for SOC, similar to recent calculations of the excess density SOC in the lower mantle [38, 39]. We therefore focus here on the results of case RCY (Table. 4, which features a buoyancy number of 0.66. RCY is an incompressible mantle circulation simulation in which oceanic crust is generated by melting at the surface (see Methods, 6.1, [32]). Shear-wave velocity anomalies (δV_s, Fig. 1c,f,i) are predicted from the temperature (Fig. 1a,d,g) and bulk composition (Fig. 1b,e,h) of the simulation by assuming that the bulk composition C of the tracer fields represents a mechanical mixture of harzburgite ($C = 0.0$), lherzolite ($C = 0.2$), and basalt ($C = 1.0$) (see Methods 6.3 for justification and further details). SOC is denser than the ambient mantle [38, 40, 41] (modelled with a positive buoyancy number, see Methods 6.1, Table 4), so it accumulates above the CMB [5, 15, 18] and is swept around by downwellings. Simulation RCY predicts present-day accumulations of SOC in the lower mantle under the Pacific and Southern Ocean (Fig. 1h) and distinctly hot regions beneath the Pacific and southern Africa (Fig. 1g), where plumes are preferentially formed (Fig. 1a,d). Converting the temperature and composition structure to seismic velocities (see Methods 6.3.1) and adjusting for the tomographic resolution (see Methods 6.4) using seismic tomography model S40RTS [35], we find low δV_s regions beneath Africa and the Pacific, similar to where they are observed seismically (Figs. 1c,f,i, S1). Henceforth, we refer to these regions as the simulated large low velocity provinces (S-LLVPs).

Qualitatively, the S-LLVPs are similar in shape to the observed seismic structure in S40RTS (Fig. S2). However, compared to the tomographically constrained maps, they are broader, and the Pacific S-LLVP is more spatially discontinuous (Fig. 1c,f,i), while the S-LLVP beneath Africa is connected to the Pacific S-LLVP at its southeastern tip. The shear wave velocity reduction itself is slightly smaller than in S40RTS [35], especially in the lowermost mantle (Fig. S2i,j). As we have tomographically filtered the V_s structure of the simulated mantle, we can quantify the similarity between it and the tomographically constrained maps (see Methods 6.4). A strong positive correlation between mantle structure predicted by simulation RCY and tomographic model S40RTS is found up to spherical harmonic degree 4 throughout the lower mantle (Fig. S3), with the depth averaged correlation up to spherical harmonic degree 4 being ~ 0.5. This indicates that the S-LLVPs resemble, in terms of relative location and size, seismically observed LLVPs, which are principally degree 2–3 structures [1, 42]. For simulations with different parameters (Table 4), the depth averaged correlation with S40RTS up to spherical harmonic degree 4 ranges from $0.44 - 0.60$, indicating that the shape of the S-LLVPs in our simulations is robust with respect to varying model parameters.

3 Composition and age differences between S-LLVPs

After S-LLVPs have been identified using the filtered δV_s field (Methods 6.5), raw properties are extracted from the two regions for comparison. The radial properties of the Pacific and African S-LLVPs differ in the lowermost 680 km of the mantle, but to different amounts depending on the property considered. If measured by the depth-integrated areal extent of the S-LLVPs over each radial layer (Fig. 2d), the African S-LLVP is only 5% more voluminous than the Pacific S-LLVP (Fig. 2d). Their average temperature and shear-wave velocity are also similar (Fig. 2b–c). However, the difference in composition is substantially larger. The bulk composition of the African S-LLVP, including an increased mean C in the lowermost 200 km of the mantle due to the preferential segregation of dense basalt to the CMB region, is similar to the mantle average (Fig. 2a). In contrast, the Pacific S-LLVP contains a broader range of compositions than its African counterpart (Fig. 3a-c), and consequently is

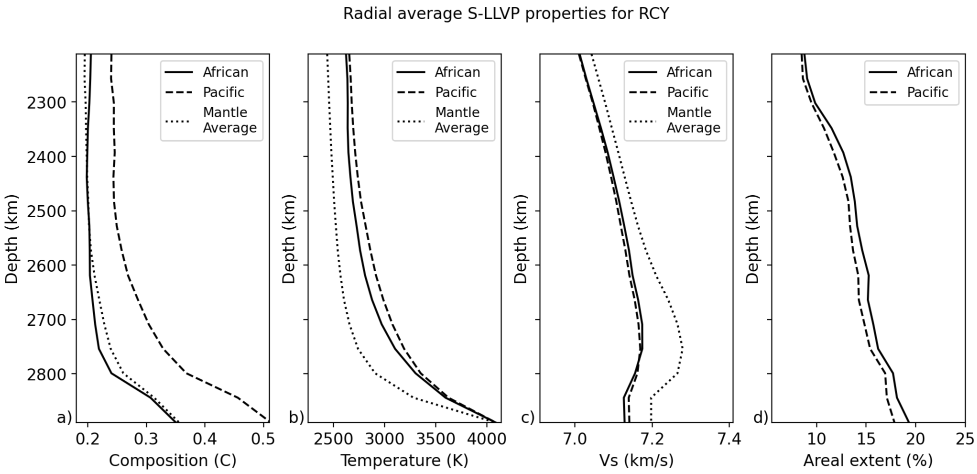

Fig. 2 Radial average S-LLVP properties in simulation RCY, showing (a) bulk composition, (b) temperature, (c) predicted absolute shear wave velocity (unfiltered) through the African S-LLVP (solid lines) and Pacific S-LLVP (dashed lines) and (d) the areal extent of each S-LLVP at each radial layer. A theoretical adiabat has been added to the temperature field to account for model incompressibility. Note that at the CMB itself, V_s is calculated using the temperature of the layer directly above as the CMB is isothermal. If the CMB temperature is used, the V_s variations would be only dependent on composition.

compositionally enriched compared to the African S-LLVP and the average mantle by up to 50%.

Enrichment of the Pacific S-LLVP in basalt is accommodated by reduced harzburgite and lherzolite fractions, with the harzburgite fraction being particularly small in the lowermost mantle (Fig. 3a). The compositional disparity between the Pacific and African S-LLVPs is also apparent in simulations with different buoyancy numbers for SOC (Fig. S4), different radial viscosity profiles in the lower mantle (Fig. S5), different CMB temperatures (Fig. S6), and also observed when using a compressible equation of state (Figs. S7, S2j-l). This implies that compositional enrichment of the Pacific S-LLVP is a robust result in our simulations and indicates that the historic pattern of downwellings strongly affects the distribution of SOC in the lower mantle [11, 12].

The melting age, defined as the average time since melting, offers an insight into the reworking history of S-LLVPs (Fig. 3f). For the African S-LLVP, the melting age distribution is mostly skewed towards older ages, with greater proportions of younger material in the lowermost ~150 km of the mantle. This implies that much of the constituent material of the African S-LLVP has been sequestered in the lower mantle for ~1 Gyr. Conversely, through the Pacific S-LLVP we observe a Gaussian distribution centered on an age of 750 Myr down to ~2600 km depth, while at greater depths the melting ages are skewed to lower values (Fig. 3f). This suggests that on average the constituent material of the African S-LLVP is older than in the Pacific S-LLVP, and that there has been a large and recent influx of young SOC into the base of the Pacific S-LLVP. An explanation for this could be that the African S-LLVP was formed prior to

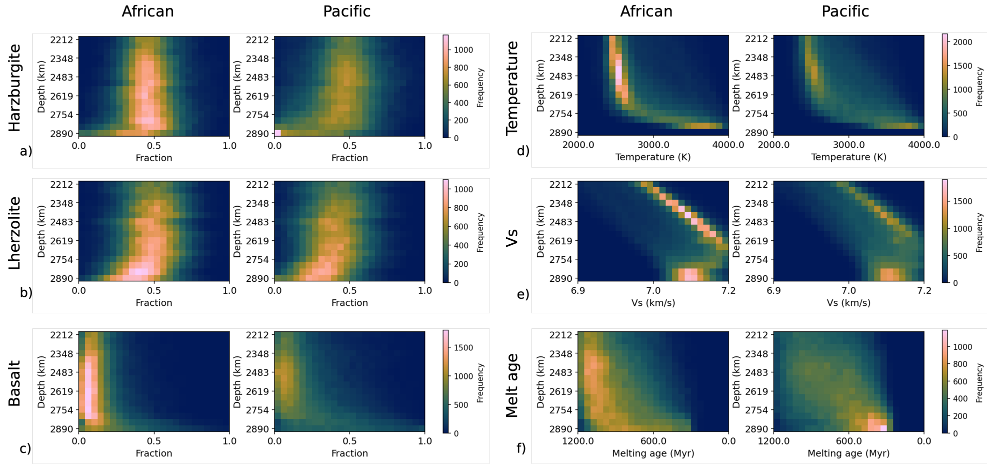

Fig. 3 Histograms for bulk composition, temperature, shear-wave velocity (V_s, unfiltered), and melting age of the African (left plot in each panel) and Pacific (right plot in each panel) S-LLVPs. The bulk composition is defined by the proportions of (a) harzburgite, (b) lherzolite, and (c) basalt. We also plot the (d) temperature, (e) predicted absolute shear wave velocity, and (f) melting age distributions. Due to the isothermal boundary condition of the simulation at the CMB, the temperature is not plotted here and the V_s in the lowermost layer is calculated using the temperature structure from the layer directly above.

the Pacific S-LLVP. Alternatively, it is possible that the Pacific S-LLVP preferentially accumulates young material compared to the African S-LLVP.

Our mantle circulation simulations enable us to assess how the subducted oceanic crust accumulates (Figure 4) and how it has been redistributed by mantle circulation in the past 1 Gyr [11]. In simulation RCY, a large volume of SOC converges in the northern hemisphere between 900 and 800 Ma. Between 800 and 600 Ma this accumulation begins to split while new SOC enters the lower mantle from subduction primarily at mid to low latitudes. From 600 to 400 Ma the subduction zones migrate into a circum-planetary girdle and the accompanying downwellings drive SOC away from these regions. At 300 Ma strong lateral flow brings SOC under the present-day Pacific region, while weak flow beneath present-day Africa allows SOC accumulations to move slowly south. From 200 Ma to present day, SOC continues to be added beneath the Pacific region, replacing the material that was lost through entrainment and advective removal, as implied by the melting age distribution (Fig. 3f). A steady rate of replenishment of young SOC [15, 30] therefore enables the Pacific S-LLVP to be maintained. Accumulations of SOC beneath present-day Africa continue to migrate south and are almost completely removed from the lowermost mantle, except beneath the Southern Ocean. A possible mechanism for the preferential addition of SOC beneath the Pacific rather than Africa is that relatively dense crust atop the oceanic lithosphere causes slabs subducted around the Pacific to overturn and fall towards the centre of the subduction girdle. As material is removed from the Pacific S-LLVP it is replaced by this SOC. In contrast, material removed from the African S-LLVP in the last ~200 Myr is replaced with older, better mixed material compared to the Pacific (Figs. 4,5).

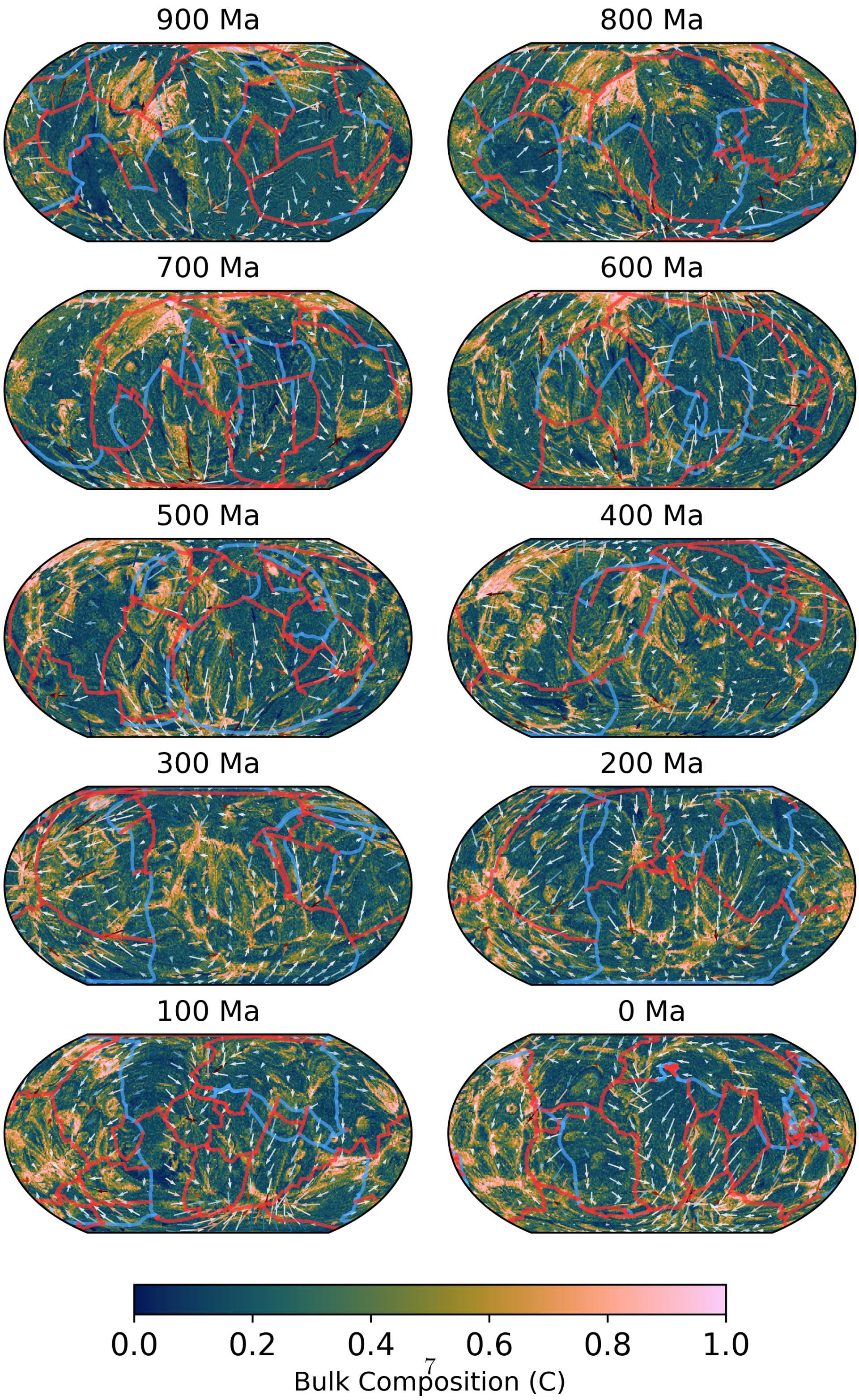

Fig. 4 Depth slices at 2844 km depth at 100 Myr intervals from 900 Ma to present day for case RCY, coloured by bulk composition. Red and blue lines indicate ridges and subduction zones respectively, as defined by the plate reconstruction used for the surface boundary condition [31]. Arrows indicate direction and magnitude of horizontal flow at 2844 km depth, coloured by the radial velocity with blues indicating downward flow (toward CMB) and reds indicating upward flow (toward surface).

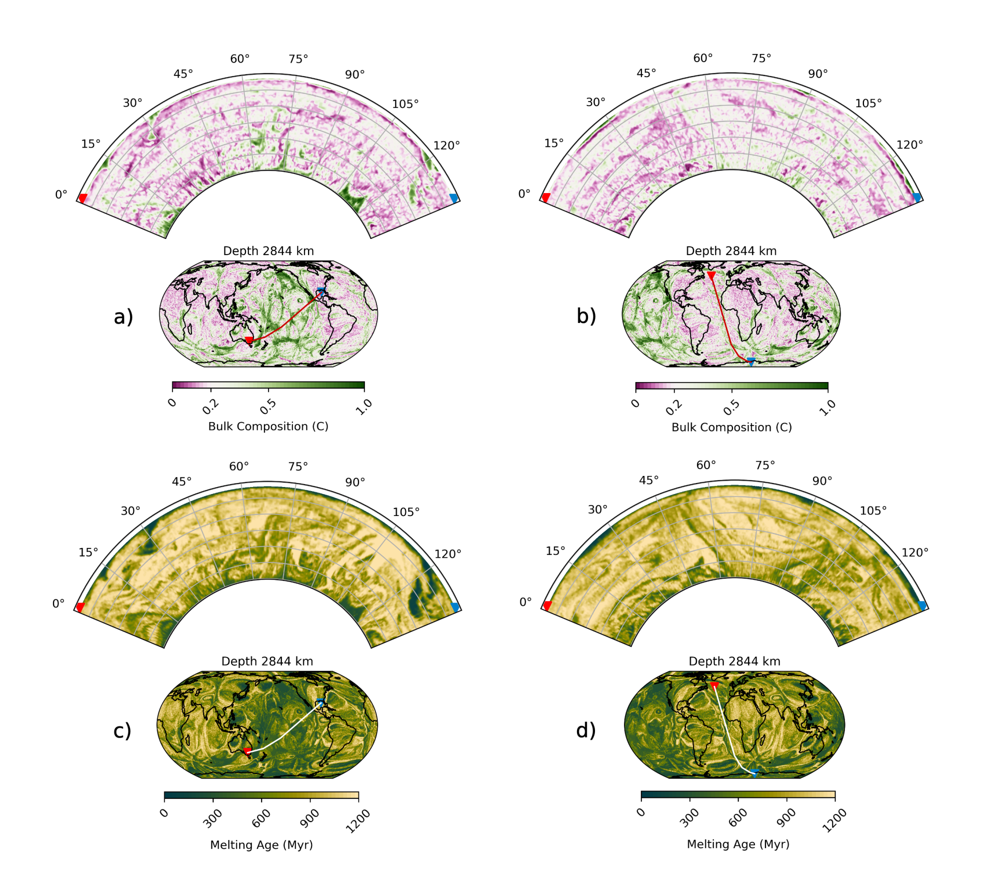

Fig. 5 Cross sections through the simulated mantle of case RCY coloured by a,b) bulk composition and c,d) melting age (average time since last melting). Inset map shows the location of the cross sections with red and blue triangles indicating the start / end of the cross section. Cross section locations have been chosen to pass through the a,c) Pacific S-LLVP and b,d) the African S-LLVP. Colour scale for bulk composition is centered on $C = 0.2$ which is the average composition for the mantle, with purple colours indicating depleted material and green colour indicating enriched material.

Due to its relatively high concentration of basaltic material (Fig. 3c), the Pacific S-LLVP is up to +1% more dense [38, 41] than the African S-LLVP. This intrinsic density is likely a controlling factor on LLVP height, with the African LLVP being more buoyant and therefore more unstable [21]. This is consistent with seismic evidence that the African LLVP extends $500-1000$ km higher into the mantle than the Pacific LLVP [19, 20, 43, 44]. Our results imply that compositional and intrinsic density differences between the two LLVPs are a natural consequence of time-varying mantle flow and different time-integrated replenishment rates.

4 Discussion

Changes in subduction zone orientation and the transport of subducted oceanic crust into the lower mantle over the past billion years have given rise to the present day extent and unique histories of the S-LLVPs (Fig. 4) [see also 11–13]. The resulting combined areal extent of the African and Pacific S-LLVPs in simulation RCY increases from 17% at 2212 km depth to 37% at the CMB (Fig. 2), making them laterally more extensive than LLVPs in tomographic images. This is likely due to a combination of factors including an imperfect representation of historic subduction zones in the plate reconstruction model and unrealistic lower mantle viscosities. In this study we also do not explicitly consider the effects of composition-dependent viscosity, which would affect the stability of basal mantle structure [45], potentially making it easier for downwellings to sculpt the S-LLVPs.

The compositional enrichment of the Pacific S-LLVP appears inconsistent with recent geochemical inferences that enriched mantle (EM) type hotspots are more closely associated with the African LLVP [22]. However, in simulation RCY the mean bulk composition of plumes associated with the two S-LLVPs shows relatively little variation ($< 30\%$, Fig. S9) given the compositional difference between the S-LLVPs (Fig. 2a), possibly because plumes form and preferentially entrain material from the edges of S-LLVPs [46]. The mean plume composition of the two domains also converges towards the surface, possibly due to increased mixing at shallower depths. We note that our simulations do not include recycling of continental crust, and we thus do not expect to explain all of the compositional complexities observed in mantle plumes.

Despite the strong compositional contrast between the African and Pacific S-LLVPs (Figs. 2a, 3a-c), their predicted radially averaged temperature and V_s differ by only 3.9% and 0.2% with respect to one another (Fig2b,c). This is because of the dominant effect of temperature compared to composition on the V_s of lower mantle minerals, which is a consequence of the mineral physics dataset used in our study (see Methods 6.3.2, Fig. S10).

Recent work suggests that in order to fit multiple robust geophysical constraints, such as dynamic topography, the geoid and normal-mode frequency variations, LLVPs may be enriched in denser than average material at their base [7, 47], with chondrite enriched basalt (CEB) proposed as a possible composition for this material. Since our study is limited to mantle circulation over the past billion years for which plate reconstruction models are available, it is not feasible to incorporate the recycling of CEB during the Hadean [7] in our simulations. However, we can approximate this situation by starting a simulation at 1.2 Ga with a 150 km thick layer of dense material at the base of the mantle with a unique ($C = 2.0$) composition (simulation PRM, Table 2). Also in this case, the Pacific S-LLVP is enriched in SOC compared to the African S-LLVP (Fig. S8c) and it is additionally enriched in primordial component (Fig. S8d). At the base of the mantle, this enhances the reduction in shear-wave velocity, making it similar to that observed in seismic tomography (Fig. S2i), compared to simulation RCY which underestimates the shear-wave reduction (Fig. S2a-f). However, at shallower depths the velocity reduction in simulation PRM is greater than observed in tomography (Fig. S2g,h). Given the more Earth-like shear-velocity reductions that can be achieved at the base of the S-LLVPs where they are enriched in CEB, we cannot rule out that primordial, chemically distinct material is present at the base of LLVPs, possibly buried and trapped at the base of the mantle by SOC [48, 49].

The incompressible approximation likely contributes to the relatively low amplitude δV_s of the S-LLVPs compared to tomographic observations. To account for the incompressibility, we add a theoretical adiabat to the simulations, scaling the temperature at each depth by the same value. Consequently, the temperature range at each depth is constant, leading potentially to reduced shear wave velocity variations in the lowermost mantle compared to compressible mantle circulation calculations. However, our tests using a compressible mantle circulation simulation (COMP), indicate that the velocity reductions in the S-LLVPs are not significantly different from those in simulation RCY (Fig. S2d,h,l). The compressible simulation is also similar to simulation RCY in producing a Pacific S-LLVP that is enriched in SOC compared to the African S-LLVP (Fig. S7a). A further source of error in estimating seismic velocities comes from the choice of the thermodynamic database [50], which does not include the iron spin transition in the lower mantle [51–53] and differs from an earlier version [37]. This reflects the fact that the determination of seismic velocities at lower mantle pressures and temperature remains difficult due to experimental challenges under extreme conditions.

5 Conclusions

Our models of mantle circulation over the past billion years demonstrate that S-LLVPs develop as a consequence of recycling oceanic crust. When evolving in this way, the Pacific and African S-LLVP have different compositions, but exhibit similar shear-wave velocity reductions due to the strong influence of temperature on V_s compared to composition. Differences in composition between the African and Pacific S-LLVPs are explained by their unique reworking histories, which are governed by the historic pattern of subduction. Melting ages indicate that the material in the African S-LLVP is mostly old and well mixed, while the material in the Pacific S-LLVP is younger and maintained by constant replenishment of young subducted oceanic crust. Our results support the idea that the top of the African LLVP is higher than the Pacific LLVP due to a smaller density contrast with the surrounding mantle. Further studies should investigate the possibility that LLVPs are particularly enriched in high density primordial material at their bases.

6 Methods

6.1 Dynamic simulations

The simulations presented in this study have been run using the three-dimensional mantle convection code, TERRA [27, 28, 54, 55]. Under the Boussinesq approximation and assuming an incompressible mantle [56], the equations for conservation of mass, momentum and energy are

$$\nabla \cdot \boldsymbol{u} = 0 \tag{1}$$

$$\nabla \cdot \left(\eta \left\{\nabla \boldsymbol{u} + (\nabla \boldsymbol{u})^T\right\}\right) - \nabla p = \boldsymbol{g}\, \alpha\, \rho_0 \left(\delta T - C\, B\, \Delta T\right) \tag{2}$$

Table 1 Common parameters to all simulations and their values. Reference viscosity is equal to the viscosity of the upper mantle.

Symbol	Parameter	Value	Unit
T_s	Surface temperature	300	K
η_0	Reference viscosity	4x10^{21}	$Pa\,s$
ρ_0	Reference density	4500	$kg\,m^{-3}$
k	Thermal conductivity	4	$W\,m^{-1}K^{-1}$
α	Thermal expansivity	2.5x10^{-5}	K^{-1}
C_p	Specific heat capacity	1100	$J\,kg^{-1}K^{-1}$

$$\rho_0\, C_p \left(\frac{\partial T}{\partial t} + \mathbf{u} \cdot \nabla T \right) - k\, \nabla^2 T - H = 0 \tag{3}$$

respectively, where $\boldsymbol{u}$ is fluid velocity, η is dynamic viscosity, T is temperature, p is dynamic pressure, $\boldsymbol{g}$ is the acceleration due to gravity, α is the coefficient of thermal expansion, ρ_0 is the reference density, C is the bulk composition (ranging between 0 and 1), B is the buoyancy number, ΔT is the temperature contrast across the mantle, t is time, C_p is the specific heat capacity constant pressure, k is thermal conductivity, H is the radiogenic heat production per unit volume and $\delta t = (T - T_{ref})$ where T_{ref} is our reference temperature profile. The buoyancy number is defined as

$$B = \frac{\Delta \rho_b}{\alpha \rho_0 \Delta T} \tag{4}$$

where $\Delta\rho_b$ is the intrinsic density difference between basalt ($C = 1$) and lherzolite ($C = 0.2$, average mantle) in the lower mantle.

The advection of bulk composition is described as

$$\frac{\partial C}{\partial t} = -\nabla \cdot (C\mathbf{u}) \tag{5}$$

as in van Heck et al. [32]. The model domain is discretized into 65 concentric layers, each composed of a regular icosahedron that is projected onto a sphere, with a radial spacing of ∼45 km. At each radial layer the icosahedron is sub-divided leading to an average lateral resolution at the surface and CMB of ∼60 km and ∼33 km respectively [27]. The model parameters and parameter values are listed in Table 1 and Table 4.

From an initial temperature distribution, the simulation is allowed to evolve for 2 Gyr with a free-slip surface boundary condition in a pre-conditioning phase. This ensures that any signal from the initial thermal structure is removed. We then run the conditioning phase whereby the first stage of the plate motion reconstruction [31] acts as the surface velocity boundary condition. This is applied for 200 Myr in order to introduce temperature, velocity and compositional structures into the mantle that reflect the overlying plate assemblage. Finally, each simulation is run forwards in time from 1000 Ma to the present day with plate motion reconstructions determining the surface velocities.

To avoid numerical instabilities and artefacts, the reference viscosity used in our simulations (Table 1), is higher than what is expected for Earth's upper mantle by approximately a factor of 4. Consequently, the RMS surface velocities in our simulations are slower than would be expected from the plate motion reconstructions. The RMS surface velocity during the pre-conditioning phase is ∼2.5 cm/yr, about 1/2 of what is estimated for the present day RMS surface velocity for plates on Earth [31]. Therefore, we apply a scaling factor of 1/2 to the reconstructed plate velocities so that they better match the flow velocities in our simulations, i.e. the reconstructed plate velocities are reduced by 50%. To maintain the correct volume flux of material through ridges and trenches, we also apply a scaling factor to the time t, increasing the model time of our simulation by a factor of 2. This scaling of parameters ensures that the simulated mantle experiences approximately the correct number of overturns for the given length of the plate reconstruction used, despite the higher than expected reference viscosity.

Viscosity in the simulations depends on depth and temperature according to:

$$\eta = \eta_z \exp((z' V_a) - (E_a T')) \tag{6}$$

where η is the viscosity, η_z is the reference viscosity (η_0) multiplied by the radial viscosity factor (Fig. S11) at depth z, z' is the non-dimensional depth, V_a=1.0 and E_a=2.0 are non-dimensional constants that control the sensitivity of viscosity to depth and temperature, and T' is the non-dimensional temperature. Depth is non-dimensionalised by $z' = z/h$, where h is the thickness of the mantle. Temperature is non-dimensionalised by $T' = (T - T_s)/(T_c - Ts)$, where T is the mantle temperature at a given point, T_s is the temperature of the surface boundary, and T_c is the temperature of the lower boundary at the CMB.

All profiles for η_z feature a strong lithosphere with a thickness of 135 km, a weak upper mantle, and a 30× viscosity jump across the 660-km discontinuity [57]. In the lower mantle, we use three profiles (Fig. S11) to explore different causes for an increase of the viscosity with depth, assuming it to be either due to increasing bridgmanite concentrations or increasing strength of ferropericlase with depth. In the lowermost mantle the radial viscosity profile also features a reduction to approximate the decrease in viscosity associated with the lower mantle bridgmanite to post-perovskite phase transition [14].

6.2 Particles

6.2.1 Bulk composition parameterization

We use tracer particles to track bulk composition and abundance of heat producing elements. Simplified bulk composition is stored as a value (C) that varies between $C = 0.0$, representing completely depleted material (harzburgite), and $C = 1.0$, representing completely enriched material (basalt), while we consider the bulk silicate Earth composition to be lherzolite. Together, these three compositions represent the characteristic lithologies of the mantle. They are each assigned a bulk composition composed of six major oxides (Table 2), with proportions chosen to fit results from Baker and Beckett [58] for harzburgite, Walter [59] for lherzolite and White and Klein [60] for basalt. To determine the C-value of lherzolite, we find the best fit vector between

Table 2 Assumed molar composition for our three standard characteristic lithologies (harzburgite, lherzolite, basalt) as well as the 'primitive' composition (CEB).

	Harzburgite	Lherzolite	Basalt	CEB
SiO2	36.184	38.819	52.298	48.47
MgO	56.559	49.894	15.812	20.00
FeO	5.954	6.145	7.121	11.28
CaO	0.889	2.874	13.027	10.59
Al2O3	0.492	1.963	9.489	11.28
Na2O	0.001	0.367	2.244	1.50

the major element mass proportions of harzburgite, lherzolite and basalt, finding this to be $C = 0.2$. Different choices for the bulk composition of basalt, harzburgite and lherzolite result in slightly different values of C (ca. 0.18–0.21 mass fraction basalt).

At the start of the pre-conditioning phase, each cell is initialised with 10 particles, with $1 \times C = 1.0$ particle, $5 \times C = 0.2$ particles and $4 \times C = 0.0$ particles, giving a mean mantle composition of $C = 0.2$.

6.2.2 Solid phase transitions in the geodynamic simulations

In our geodynamic simulations, we use a simplified parameterization of the phase transitions in the olivine system, which occur at 410 and 660 km depth (Table 3). This parameterization allows us to reproduce some of the behaviour associated with these discontinuities [33, 61]. The depth and bulk composition of particles affects the density field, which is quantified by the buoyancy number (Equation 4). We vary the buoyancy number in some simulations (Table 4) to investigate the effect of different intrinsic densities of SOC [30], for which estimates vary between 0.5 and 5% more dense than average mantle [38, 41, 62].

6.2.3 Melting in the geodynamic simulations

A linear solidus, dependent on depth (z) and bulk composition, controls melting in the simulations [30, 32, 33]:

$$T_{\text{solidus}}(z, C) = T_{\text{meltsurf}} + zT_{\text{meltslope}} + (1 - C)T_{\text{meltcomp}} \tag{7}$$

where $T_{\text{meltsurf}} = 1200$ K is the melting temperature of basalt ($C = 1$) at the surface, $T_{\text{meltslope}} = 2.5$ K km^{-1} is the gradient of the solidus and $T_{\text{meltcomp}} = 500$ K is the temperature difference between the solidi of basalt ($C = 1$) and harzburgite ($C = 0$). At each time step, we check whether particles in the uppermost 135 km have crossed their solidus. If this is the case, the melting particle has its bulk composition reduced so that it plots on the solidus for the particle's temperature and pressure until it cannot be further depleted ($C = 0$). Particles at the surface are enriched with the produced melt, assuming instantaneous melt migration. Full details of this melting process in the dynamic simulations can be found in refs. [30, 32, 34].

Table 3 Olivine phase change parameters for an assumed composition with 67% $(\mathrm{Mg,Fe})_2\,\mathrm{SiO}_4$.

Depth (km)	**$\Delta\rho$ kg m^{-3}**	**Clapeyron slope MPa K^{-1}**
410	230	2.25
660	380	-1.5

6.3 Seismic properties

6.3.1 Converting from simulation to seismic properties

We convert the pressure, temperature and composition of our simulations to seismic properties using look-up tables for each of the characteristic lithologies. Due to the incompressible equation of state used in our simulations, we add a theoretical adiabat to the simulated temperature field before performing this conversion. We use the thermodynamic data set of [50], implemented in the Perple_X software [63] to generate tables for density and effective isotropic seismic properties for each lithology in pressure - temperature space. Attenuation is accounted for using model Q7g [64, 65]. The thermodynamic data set includes all major mantle phase transitions, but does not include the spin transition in ferropericlase, nor the second order phase transition in stishovite. Although these may reduce seismic velocities in the lower mantle, the effect on the shear-wave velocity is small [53].

As the bulk composition in our simulation is tracked using only a single parameter C, it is not possible to differentiate between mechanical and equillibrated mixtures of different compositions. We therefore make a pragmatic decision for how to convert C to lithology. An important requirement is that primitive mantle is modelled as pure lherzolite, not as a mechanical mixture of basalt and harzburgite. Therefore, we model particles with a bulk composition between $C = 0.0$ and $C = 0.2$ as a mechanical mixture [66] of harzburgite and lherzolite, and particles with a bulk composition between $C = 0.2$ and $C = 1.0$ as a mechanical mixture of lherzolite and basalt. The relative proportions of each characteristic lithology are interpolated from the particles to the grid so that at each grid point we have information on the relative proportions of each of the three lithologies. Seismic properties at the grid point are then calculated by taking the harmonic mean of the properties for each lithology at the temperature and pressure of the grid point, weighted by the relative proportions of each lithology. Although our one-parameter compositional tracking and simplified geodynamic approach to phase transitions do not capture the full effects of chemical variation in the mantle, our post-processing approach is highly efficient and facilitates a detailed exploration of model parameters such as buoyancy number (excess density of SOC), independently from the thermodynamic model. This also allows us to investigate the choice of different assumed compositions independently of the geodynamic model.

6.3.2 The dominant effect of temperature on V_s

For the assumed molar compositions of the characteristic lithologies (Table 2), the predicted δV_s between lherzolite and harzburgite is small (Figs. S10a,b,d, S12) at lower mantle pressures. This is because both lherzolite and harzburgite are silica-undersaturated and are dominated by bridgmanite and ferropericlase. The V_s of basalt varies more strongly with temperature and pressure (Fig. S10c). Between 80 and 95 GPa, the V_s of basalt is about 0.1 km/s higher than that of lherzolite (Fig. S10e) and harzburgite (Fig. S10f), but with increasing pressure the V_s of basalt becomes lower than lherzolite and harzburgite across an increasingly wide temperature range. Nonetheless, the average difference in absolute V_s between harzburgite and basalt is just 0.07 km/s (about 1%). However, within the temperature range relevant to the S-LLVPs ($2200 - 4300K$, Fig. 3d), the mean of the differences between the maximum and minimum V_s at each 0.1 GPa pressure point between 80 and 140 GPa is 0.42 km/s for harzburgite and 0.40 km/s for lherzolite and basalt, i.e. about 5% variation.

As such, velocity variations are primarily determined by temperature variations in the mantle since these 5% variations due to temperature are greater than the 1% variation arising from compositional differences. The δV_s of the two S-LLVPs is thus comparable because they are both similarly hot compared to the ambient mantle (Fig.2b) [67, 68]. Compositional differences (Figs.3a-c,2a) are undetectable seismically (Fig.2c), especially if the post-perovskite transformation is suppressed (Fig. S13), though the precise details of the post-perovskite transition remain debated.

6.4 Filtering

In order to quantitatively compare the numerical simulations to seismic tomography, we follow the approach of [24], thus accounting for the limited tomographic resolution. The maps of simulated shear wave velocity variations in the mantle are first reparameterized to spherical harmonic coefficients up to degree 40 and the same 21 radial splines as in seismic tomography model S40RTS [35]. We then apply the S40RTS resolution matrix that describes how the tomographic resolution varies spatially due to the non-uniform seismic data coverage and applied model damping. The tomographic filter smooths the seismic velocity variations and suppresses amplitudes, but makes our predictions based on the simulation directly comparable with S40RTS, for example in figures 1 and S2, which show the filtered δV_s field.

6.5 Identifying low velocity domains in our simulations

To identify low velocity domains in the filtered V_s field based on our simulations, we use a K-means clustering algorithm [69]. We apply this to the filtered δV_s field at depths between 2212 - 2890 km depth to split the field into three clusters. The points in the 'low' cluster comprise the simulated large low velocity provinces (S-LLVPs). The geographic positions of these points in the model domain are then used to mask the model output fields to extract data only for points within the S-LLVPs (Fig. S1).

6.6 Additional simulations

We have run several additional simulations to support the findings presented in the main text. Specifically, we have investigated the effects of a lower buoyancy number for SOC (simulations B=0.44 and B=0.22), different radial viscosity profiles (simulations visc2 and visc3), and different CMB temperatures (simulations CMB2800 and CMB2600) on the composition and formation histories of S-LLVPs (Table 4).

Table 4 Table showing the buoyancy number, viscosity profile and CMB temperature used in each simulation. Viscosity profiles are plotted in Fig. S11.

Name	Buoyancy Number	Viscosity Profile	CMB Temperature (K)	Initial Primordial Layer Thickness (km)
RCY	0.66	visc1	3000	-
B=0.44	0.44	visc1	3000	-
B=0.22	0.22	visc1	3000	-
visc2	0.66	visc2	3000	-
visc3	0.66	visc3	3000	-
CMB2800	0.66	visc2	2800	-
CMB2600	0.66	visc2	2600	-
PRM	0.66	visc1	3000	150
COMP	0.66	visc1	4000	-

While different parameter combinations have an effect on the overall size and shape of the S-LLVPs, we consistently observe the same trend for each case, namely that the Pacific and African S-LLVPs have a similar radially averaged temperature and V_s structure, but that the Pacific is enriched in SOC, and in the case of PRM, also enriched in primordial material, compared to the African S-LLVP.

Acknowledgments

This work was supported by the NERC Large Grant "Mantle Circulation Constrained (MC2): A multidisciplinary 4D Earth framework for understanding mantle upwellings" (Grant NE/T012633/1). P.K. acknowledges support from a Royal Society University Research Fellowship (URF\1\180377). Numerical simulations were conducted on ARCHER2, the UK's national high-performance supercomputer. In our figures we make use of perceptually uniform colourmaps [70]. This is Cardiff EARTH CRediT Contribution 30. For the purpose of open access, the author has applied a CC BY public copyright licence to any Author Accepted Manuscript version arising.

Funding

This work was supported by NERC grant number NE/T012633/1 and Royal Society grant URF\1\180377.

Competing Interests

The authors declare no competing interests

Data availability

Simulation outputs for this study can be accessed at 10.5281/zenodo.11222080.

Code availabilty

The code TERRA used in this study is not freely available as the code predates open-source licensing. As such we do not have the rights to release all parts of the code, however code pieces which have been implemented for this study are available at 10.5281/zenodo.11222080 along with code for reproducing analysis carried out in this study. We also make use of the terratools (10.5281/zenodo.10797185) package in the analysis of simulation results. The Perple_X code to generate mineral physics lookup tables [63] is available at www.perplex.ethz.ch/. Code used for tomographic filtering of model results [24] can be found at www.earth.ox.ac.uk/∼niv4152/downloads_filtering.html.

Authors contributions

JP: Conceptualisation, methodology, software, validation, formal analysis, investigation, data curation, writing (original draft), writing (review & editing), visualisation **HD**: Conceptualisation, resources, writing (review & editing), supervision, project administration, validation, funding acquisition **PK**: Software, writing (review & editing), validation, funding acquisition **JR**: Software, writing (review & editing) **RM**: Software, writing (review & editing).

References

[1] Ritsema, J., Lekić, V.: Heterogeneity of seismic wave velocity in earth's mantle. Annual Review of Earth and Planetary Sciences **48**(1), 377–401 (2020) https://doi.org/10.1146/annurev-earth-082119-065909

[2] Li, X.-D., Romanowicz, B.: Global mantle shear velocity model developed using nonlinear asymptotic coupling theory. Journal of Geophysical Research: Solid Earth **101**(B10), 22245–22272 (1996) https://doi.org/10.1029/96JB01306 . _eprint: https://onlinelibrary.wiley.com/doi/pdf/10.1029/96JB01306. Accessed 2023-03-09

[3] Garnero, E.J., McNamara, A.K., Shim, S.-H.: Continent-sized anomalous zones with low seismic velocity at the base of Earth's mantle. Nature Geoscience **9**(7), 481–489 (2016) https://doi.org/10.1038/ngeo2733 . Number: 7 Publisher: Nature Publishing Group. Accessed 2023-03-09

[4] Davies, D.R., Goes, S., Lau, H.C.P.: Thermally Dominated Deep Mantle LLSVPs: A Review. In: Khan, A., Deschamps, F. (eds.) The Earth's Heterogeneous Mantle: A Geophysical, Geodynamical, and Geochemical Perspective, pp. 441–477. Springer, Cham (2015). https://doi.org/10.1007/978-3-319-15627-9_14 . https://doi.org/10.1007/978-3-319-15627-9_14

[5] Jones, T.D., Maguire, R.R., Van Keken, P.E., Ritsema, J., Koelemeijer, P.: Subducted oceanic crust as the origin of seismically slow lower-mantle structures. Progress in Earth and Planetary Science **7**, 17 (2020) https://doi.org/10.1186/s40645-020-00327-1

[6] Niu, Y., Wilson, M., Humphreys, E.R., O'Hara, M.J.: A trace element perspective on the source of ocean island basalts (OIB) and fate of subducted ocean crust (SOC) and mantle lithosphere (SML). Episodes Journal of International Geoscience **35**(2), 310–327 (2012) https://doi.org/10.18814/epiiugs/2012/v35i2/002 . Publisher: International Union of Geological Sciences

[7] Richards, F.D., Hoggard, M.J., Ghelichkhan, S., Koelemeijer, P., Lau, H.C.P.: Geodynamic, geodetic, and seismic constraints favour deflated and dense-cored LLVPs. Earth and Planetary Science Letters **602**, 117964 (2023) https://doi.org/10.1016/j.epsl.2022.117964 . Accessed 2023-03-02

[8] Zhang, Z., Dorfman, S.M., Labidi, J., Zhang, S., Li, M., Manga, M., Stixrude, L., McDonough, W.F., Williams, Q.: Primordial metallic melt in the deep mantle. Geophysical Research Letters **43**(8), 3693–3699 (2016) https://doi.org/10.1002/2016GL068560 . _eprint: https://onlinelibrary.wiley.com/doi/pdf/10.1002/2016GL068560

[9] Gleeson, M., Soderman, C., Matthews, S., Cottaar, S., Gibson, S.: Geochemical Constraints on the Structure of the Earth's Deep Mantle

and the Origin of the LLSVPs. Geochemistry, Geophysics, Geosystems **22**(9), 2021–009932 (2021) https://doi.org/10.1029/2021GC009932 . _eprint: https://onlinelibrary.wiley.com/doi/pdf/10.1029/2021GC009932. Accessed 2023-03-07

[10] Bower, D.J., Gurnis, M., Seton, M.: Lower mantle structure from paleogeographically constrained dynamic Earth models. Geochemistry, Geophysics, Geosystems **14**(1), 44–63 (2013) https://doi.org/10.1029/2012GC004267 . _eprint: https://onlinelibrary.wiley.com/doi/pdf/10.1029/2012GC004267. Accessed 2023-03-08

[11] Cao, X., Flament, N., Müller, R.D.: Coupled Evolution of Plate Tectonics and Basal Mantle Structure. Geochemistry, Geophysics, Geosystems **22**(1), 2020–009244 (2021) https://doi.org/10.1029/2020GC009244 . _eprint: https://onlinelibrary.wiley.com/doi/pdf/10.1029/2020GC009244. Accessed 2023-03-08

[12] Grabreck, A., Flament, N., Bodur, F.: Mapping global kimberlite potential from reconstructions of mantle flow over the past billion years. PLOS ONE **17**(6), 0268066 (2022) https://doi.org/10.1371/journal.pone.0268066 . Publisher: Public Library of Science. Accessed 2023-03-07

[13] Cao, X., Flament, N., Bodur, F., Müller, R.D.: The evolution of basal mantle structure in response to supercontinent aggregation and dispersal. Scientific Reports **11**(1), 22967 (2021) https://doi.org/10.1038/s41598-021-02359-z . Number: 1 Publisher: Nature Publishing Group. Accessed 2023-03-08

[14] Li, Y., Deschamps, F., Tackley, P.J.: The stability and structure of primordial reservoirs in the lower mantle: insights from models of thermochemical convection in three-dimensional spherical geometry. Geophys. J. Int. **199**(2), 914–930 (2014) https://doi.org/10.1093/gji/ggu295

[15] Mulyukova, E., Steinberger, B., Dabrowski, M., Sobolev, S.V.: Survival of LLSVPs for billions of years in a vigorously convecting mantle: Replenishment and destruction of chemical anomaly. Journal of Geophysical Research: Solid Earth **120**(5), 3824–3847 (2015) https://doi.org/10.1002/2014JB011688 . Publisher: Blackwell Publishing Ltd

[16] Li, M., McNamara, A.K.: The difficulty for subducted oceanic crust to accumulate at the earth's core-mantle boundary. Journal of Geophysical Research: Solid Earth **118**(4), 1807–1816 (2013) https://doi.org/10.1002/jgrb.50156

[17] Huang, C., Leng, W., Wu, Z.: The continually stable subduction, iron-spin transition, and the formation of llsvps from subducted oceanic crust. Journal of Geophysical Research: Solid Earth **125**(1), 2019–018262 (2020) https://doi.org/10.1029/2019JB018262 . _eprint: https://onlinelibrary.wiley.com/doi/pdf/10.1029/2019JB018262

[18] Christensen, U.R., Hofmann, A.W.: Segregation of subducted oceanic crust in the convecting mantle. Journal of Geophysical Research: Solid Earth **99**(B10), 19867–19884 (1994) https://doi.org/10.1029/93JB03403 . ISBN: 2156-2202

[19] Wang, Y., Wen, L.: Geometry and P and S velocity structure of the “African Anomaly”. Journal of Geophysical Research: Solid Earth **112**(B5) (2007) https://doi.org/10.1029/2006JB004483 . _eprint: https://onlinelibrary.wiley.com/doi/pdf/10.1029/2006JB004483. Accessed 2023-07-12

[20] He, Y., Wen, L.: Structural features and shear-velocity structure of the “Pacific Anomaly”. Journal of Geophysical Research: Solid Earth **114**(B2) (2009) https://doi.org/10.1029/2008JB005814 . _eprint: https://onlinelibrary.wiley.com/doi/pdf/10.1029/2008JB005814. Accessed 2023-07-12

[21] Yuan, Q., Li, M.: Instability of the African large low-shear-wave-velocity province due to its low intrinsic density. Nature Geoscience **15**(4), 334–339 (2022) https://doi.org/10.1038/s41561-022-00908-3 . Number: 4 Publisher: Nature Publishing Group. Accessed 2023-02-09

[22] Doucet, L.S., Li, Z.-X., Gamal El Dien, H., Pourteau, A., Murphy, J.B., Collins, W.J., Mattielli, N., Olierook, H.K.H., Spencer, C.J., Mitchell, R.N.: Distinct formation history for deep-mantle domains reflected in geochemical differences. Nature Geoscience **13**(7), 511–515 (2020) https://doi.org/10.1038/s41561-020-0599-9 . Number: 7 Publisher: Nature Publishing Group. Accessed 2023-03-07

[23] Jackson, M.G., Becker, T.W., Steinberger, B.: Spatial Characteristics of Recycled and Primordial Reservoirs in the Deep Mantle. Geochemistry, Geophysics, Geosystems **22**(3), 2020–009525 (2021) https://doi.org/10.1029/2020GC009525 . _eprint: https://onlinelibrary.wiley.com/doi/pdf/10.1029/2020GC009525. Accessed 2023-03-08

[24] Ritsema, J., McNamara, A.K., Bull, A.L.: Tomographic filtering of geodynamic models: Implications for models interpretation and large-scale mantle structure. Journal of Geophysical Research: Solid Earth **112**(1) (2007) https://doi.org/10.1029/2006JB004566

[25] Ritsema, J., Van Heijst, H.J., Woodhouse, J.H., Deuss, A.: Long-period body wave traveltimes through the crust: implication for crustal corrections and seismic tomography. Geophysical Journal International **179**(2), 1255–1261 (2009) https://doi.org/10.1111/j.1365-246X.2009.04365.x . Accessed 2024-04-26

[26] Jackson, M.G., Becker, T.W., Konter, J.G.: Geochemistry and Distribution of Recycled Domains in the Mantle Inferred From Nd and Pb Isotopes in Oceanic Hot Spots: Implications for Storage in the Large

Low Shear Wave Velocity Provinces. Geochemistry, Geophysics, Geosystems **19**(9), 3496–3519 (2018) https://doi.org/10.1029/2018GC007552 . _eprint: https://onlinelibrary.wiley.com/doi/pdf/10.1029/2018GC007552. Accessed 2023-03-08

[27] Baumgardner, J.R.: Three-dimensional treatment of convective flow in the earth's mantle. Journal of Statistical Physics **39**(5-6), 501–511 (1985) https://doi.org/10.1007/BF01008348

[28] Bunge, H.-P., Baumgardner, J.R.: Mantle convection modeling on parallel virtual machines. Computers in Physics **9**(2), 207 (1995) https://doi.org/10.1063/1.168525

[29] Bunge, H.-P., Baumgardner, J.R.: Mantle convection modeling on parallel virtual machines. Computers in Physics **9**(2), 207 (1995) https://doi.org/10.1063/1.168525

[30] Panton, J., Davies, J.H., Myhill, R.: The Stability of Dense Oceanic Crust Near the Core-Mantle Boundary. Journal of Geophysical Research: Solid Earth **128**(2), 2022–025610 (2023) https://doi.org/10.1029/2022JB025610 . _eprint: https://onlinelibrary.wiley.com/doi/pdf/10.1029/2022JB025610. Accessed 2023-03-09

[31] Müller, R.D., Flament, N., Cannon, J., Tetley, M.G., Williams, S.E., Cao, X., Bodur, F., Zahirovic, S., Merdith, A.: A tectonic-rules-based mantle reference frame since 1 billion years ago – implications for supercontinent cycles and plate–mantle system evolution. Solid Earth **13**(7), 1127–1159 (2022) https://doi.org/10.5194/se-13-1127-2022 . Publisher: Copernicus GmbH. Accessed 2023-02-13

[32] Heck, H.J., Davies, J.H., Elliott, T., Porcelli, D.: Global-scale modelling of melting and isotopic evolution of Earth's mantle: Melting modules for TERRA. Geoscientific Model Development **9**(4), 1399–1411 (2016) https://doi.org/10.5194/gmd-9-1399-2016

[33] Price, M.G., Davies, J.H., Panton, J.: Controls on the Deep-Water Cycle Within Three-Dimensional Mantle Convection Models. Geochemistry, Geophysics, Geosystems **20**(5) (2019) https://doi.org/10.1029/2018GC008158

[34] Panton, J., Davies, J.H., Elliott, T., Andersen, M., Porcelli, D., Price, M.G.: Investigating Influences on the Pb Pseudo-Isochron Using Three-Dimensional Mantle Convection Models With a Continental Reservoir. Geochemistry, Geophysics, Geosystems **23**(8), 2021–010309 (2022) https://doi.org/10.1029/2021GC010309 . _eprint: https://onlinelibrary.wiley.com/doi/pdf/10.1029/2021GC010309. Accessed 2023-03-09

[35] Ritsema, J., Deuss, A., Van Heijst, H.J., Woodhouse, J.H.: S40RTS: A degree-40 shear-velocity model for the mantle from new Rayleigh wave dispersion, teleseismic traveltime and normal-mode splitting function measurements. Geophysical Journal International **184**(3), 1223–1236 (2011) https://doi.org/10.1111/J.1365-246X.2010.04884.X

[36] Hosseini, K., Matthews, K.J., Sigloch, K., Shephard, G.E., Domeier, M., Tsekhmistrenko, M.: SubMachine: Web-Based Tools for Exploring Seismic Tomography and Other Models of Earth's Deep Interior. Geochemistry, Geophysics, Geosystems **19**(5), 1464–1483 (2018) https://doi.org/10.1029/2018GC007431 . _eprint: https://onlinelibrary.wiley.com/doi/pdf/10.1029/2018GC007431. Accessed 2023-07-07

[37] Stixrude, L., Lithgow-Bertelloni, C.: Thermodynamics of mantle minerals - II. Phase equilibria. Geophysical Journal International **184**(3), 1180–1213 (2011) https://doi.org/10.1111/j.1365-246X.2010.04890.x https://academic.oup.com/gji/article-pdf/184/3/1180/27638878/184-3-1180.pdf

[38] Wang, W., Xu, Y., Sun, D., Ni, S., Wentzcovitch, R., Wu, Z.: Velocity and density characteristics of subducted oceanic crust and the origin of lower-mantle heterogeneities. Nature Communications 2020 11:1 **11**(1), 1–8 (2020) https://doi.org/10.1038/s41467-019-13720-2 . Publisher: Nature Publishing Group

[39] Tsuchiya, T.: Elasticity of subducted basaltic crust at the lower mantle pressures: Insights on the nature of deep mantle heterogeneity. Physics of the Earth and Planetary Interiors **188**(3-4), 142–149 (2011) https://doi.org/10.1016/J.PEPI.2011.06.018 . Publisher: Elsevier

[40] Ringwood, A.E., Irifune, T.: Nature of the 650–km seismic discontinuity: implications for mantle dynamics and differentiation. Nature **331**(6152), 131–136 (1988) https://doi.org/10.1038/331131a0 . ISBN: 0028-0836

[41] Hirose, K., Takafuji, N., Sata, N., Ohishi, Y.: Phase transition and density of subducted MORB crust in the lower mantle. Earth and Planetary Science Letters **237**(1-2), 239–251 (2005) https://doi.org/10.1016/j.epsl.2005.06.035 . Publisher: Elsevier

[42] Lekic, V., Cottaar, S., Dziewonski, A., Romanowicz, B.: Cluster analysis of global lower mantle tomography: A new class of structure and implications for chemical heterogeneity. Earth and Planetary Science Letters **357-358**, 68–77 (2012) https://doi.org/10.1016/j.epsl.2012.09.014

[43] Cottaar, S., Lekic, V.: Morphology of seismically slow lower-mantle structures. Geophysical Journal International **207**(2), 1122–1136 (2016) https://doi.org/10.1093/gji/ggw324 . Accessed 2023-07-12

[44] Ni, S., Tan, E., Gurnis, M., Helmberger, D.: Sharp Sides to the African Superplume. Science **296**(5574), 1850–1852 (2002) https://doi.org/10.1126/science.1070698 . Publisher: American Association for the Advancement of Science. Accessed 2023-07-12

[45] Li, Y., Deschamps, F., Tackley, P.J.: Effects of the post-perovskite phase transition properties on the stability and structure of primordial reservoirs in the lower mantle of the Earth. Earth and Planetary Science Letters **432**, 1–12 (2015) https://doi.org/10.1016/j.epsl.2015.09.040

[46] Hassan, R., Flament, N., Gurnis, M., Bower, D.J., Müller, D.: Provenance of plumes in global convection models. Geochemistry, Geophysics, Geosystems **16**(5), 1465–1489 (2015) https://doi.org/10.1002/2015GC005751 . Publisher: John Wiley & Sons, Ltd. Accessed 2022-08-04

[47] Koelemeijer, P., Deuss, A., Ritsema, J.: Density structure of Earth's lowermost mantle from Stoneley mode splitting observations. Nature Communications **8**(1), 15241 (2017) https://doi.org/10.1038/ncomms15241 . Publisher: Nature Publishing Group. Accessed 2024-03-15

[48] Jones, T.D., Sime, N., Keken, P.E.: Burying Earth's Primitive Mantle in the Slab Graveyard. Geochemistry, Geophysics, Geosystems **22**(3), 2020–009396 (2021) https://doi.org/10.1029/2020GC009396 . _eprint: https://onlinelibrary.wiley.com/doi/pdf/10.1029/2020GC009396. Accessed 2023-03-07

[49] Gülcher, A.J.P., Ballmer, M.D., Tackley, P.J.: Coupled dynamics and evolution of primordial and recycled heterogeneity in Earth's lower mantle. Solid Earth **12**(9), 2087–2107 (2021) https://doi.org/10.5194/se-12-2087-2021

[50] Stixrude, L., Lithgow-Bertelloni, C.: Thermal expansivity, heat capacity and bulk modulus of the mantle. Geophysical Journal International **228**(2), 1119–1149 (2022) https://doi.org/10.1093/gji/ggab394 . Accessed 2023-03-07

[51] Badro, J., Fiquet, G., Guyot, F., Rueff, J.-P., Struzhkin, V.V., Vankó, G., Monaco, G.: Iron partitioning in earth's mantle: Toward a deep lower mantle discontinuity. Science **300**(5620), 789–791 (2003) https://doi.org/10.1126/science.1081311 . Publisher: American Association for the Advancement of Science. Accessed 2024-03-15

[52] Ammann, M.W., Brodholt, J.P., Dobson, D.P.: Ferrous iron diffusion in ferropericlase across the spin transition. Earth and Planetary Science Letters **302**(3), 393–402 (2011) https://doi.org/10.1016/j.epsl.2010.12.031 . Accessed 2024-03-15

[53] Trautner, V.E., Stackhouse, S., Turner, A.R., Koelemeijer, P., Davies, D.R., Méndez, A.S.J., Satta, N., Kurnosov, A., Liermann, H.-P., Marquardt, H.: Compressibility of ferropericlase at high-temperature: Evidence for the iron spin

crossover in seismic tomography. Earth and Planetary Science Letters **618**, 118296 (2023) https://doi.org/10.1016/j.epsl.2023.118296 . Accessed 2024-04-26

[54] Bunge, H.-P., Richards, M.A., Baumgardner, J.R.: A sensitivity study of three-dimensional spherical mantle convection at 10 8 Rayleigh number: Effects of depth-dependent viscosity, heating mode, and an endothermic phase change. Journal of Geophysical Research: Solid Earth **102**(B6), 11991–12007 (1997) https://doi.org/10.1029/96JB03806 . ISBN: 0148-0227

[55] Bunge, H.-P., Hagelberg, C.R., Travis, B.J.: Mantle circulation models with variational data assimilation: inferring past mantle flow and structure from plate motion histories and seismic tomography. Geophysical Journal International **152**(2), 280–301 (2003) https://doi.org/10.1046/j.1365-246X.2003.01823.x . Accessed 2020-11-30

[56] McKenzie, D.P., Roberts, J.M., Weiss, N.O.: Convection in the earth's mantle: Towards a numerical simulation. Journal of Fluid Mechanics **62**(3), 465–538 (1974) https://doi.org/10.1017/S0022112074000784 . ISBN: 0022-1120

[57] Keken, P.E., Ballentine, C.J.: Whole-mantle versus layered mantle convection and the role of a high-viscosity lower mantle in terrestrial volatile evolution. Earth and Planetary Science Letters **156**(1-2), 19–32 (1998) https://doi.org/10.1016/s0012-821x(98)00023-5

[58] Baker, M.B., Beckett, J.R.: The origin of abyssal peridotites: a reinterpretation of constraints based on primary bulk compositions. Earth and Planetary Science Letters **171**(1), 49–61 (1999) https://doi.org/10.1016/S0012-821X(99)00130-2

[59] Walter, M.J.: 2.08 - Melt Extraction and Compositional Variability in Mantle Lithosphere. In: Holland, H.D., Turekian, K.K. (eds.) Treatise on Geochemistry, pp. 363–394. Pergamon, Oxford (2003). https://doi.org/10.1016/B0-08-043751-6/02008-9 . https://www.sciencedirect.com/science/article/pii/B0080437516020089 Accessed 2024-03-18

[60] White, W.M., Klein, E.M.: 4.13 - Composition of the Oceanic Crust. In: Holland, H.D., Turekian, K.K. (eds.) Treatise on Geochemistry (Second Edition), pp. 457–496. Elsevier, Oxford (2014). https://doi.org/10.1016/B978-0-08-095975-7.00315-6

[61] Wolstencroft, M., Huw Davies, J.: Breaking supercontinents; No need to choose between passive or active. Solid Earth **8**(4), 817–825 (2017) https://doi.org/10.5194/se-8-817-2017

[62] Ricolleau, A., Perrillat, J.-P., Fiquet, G., Daniel, I., Matas, J., Addad, A., Menguy, N., Cardon, H., Mezouar, M., Guignot, N.: Phase relations and equation of state of a natural MORB: Implications for the density profile of subducted oceanic crust in the Earth's lower mantle. Journal of Geophysical Research: Solid Earth

115(B8), 8202 (2010) https://doi.org/10.1029/2009JB006709 . Publisher: John Wiley & Sons, Ltd

[63] Connolly, J.a.D.: The geodynamic equation of state: What and how. Geochemistry, Geophysics, Geosystems **10**(10) (2009) https://doi.org/10.1029/2009GC002540 . _eprint: https://onlinelibrary.wiley.com/doi/pdf/10.1029/2009GC002540. Accessed 2023-04-21

[64] Goes, S., Cammarano, F., Hansen, U.: Synthetic seismic signature of thermal mantle plumes. Earth and Planetary Science Letters **218**(3), 403–419 (2004) https://doi.org/10.1016/S0012-821X(03)00680-0 . Accessed 2023-07-20

[65] Maguire, R., Ritsema, J., Keken, P.E., Fichtner, A., Goes, S.: P- and S-wave delays caused by thermal plumes. Geophysical Journal International **206**(2), 1169–1178 (2016) https://doi.org/10.1093/gji/ggw187 . Accessed 2023-07-20

[66] Xu, W., Lithgow-Bertelloni, C., Stixrude, L., Ritsema, J.: The effect of bulk composition and temperature on mantle seismic structure. Earth and Planetary Science Letters **275**(1-2), 70–79 (2008) https://doi.org/10.1016/j.epsl.2008.08.012 . ISBN: 0012-821X

[67] Davies, D.R., Goes, S., Davies, J.H., Schuberth, B.S.A., Bunge, H.P., Ritsema, J.: Reconciling dynamic and seismic models of Earth's lower mantle: The dominant role of thermal heterogeneity. Earth and Planetary Science Letters **353-354**, 253–269 (2012) https://doi.org/10.1016/j.epsl.2012.08.016 . Publisher: Elsevier ISBN: 0012-821X

[68] Davies, D.R.: Thermally dominated deep mantle LLSVPs: A review (2015) https://doi.org/10.1007/978-3-319-15627-9_14

[69] Pedregosa, F., Varoquaux, G., Gramfort, A., Michel, V., Thirion, B., Grisel, O., Blondel, M., Prettenhofer, P., Weiss, R., Dubourg, V., Vanderplas, J., Passos, A., Cournapeau, D., Brucher, M., Perrot, M., Duchesnay, : Scikit-learn: Machine Learning in Python. Journal of Machine Learning Research **12**(85), 2825–2830 (2011). Accessed 2023-07-28

[70] Crameri, F., Shephard, G.E., Heron, P.J.: The misuse of colour in science communication. Nature Communications **11**(1), 1–10 (2020) https://doi.org/10.1038/s41467-020-19160-7 . Publisher: Nature Research. Accessed 2021-01-29

Supplementary Information for: Unique composition and evolution histories of low velocity mantle domains

James Panton[1*], J. Huw Davies[1], Paula Koelemeijer[2], Jeroen Ritsema[3], Robert Myhill[4]

[1*]School of Earth and Environmental Sciences, Cardiff University, Park Place, Cardiff, CF10 3AT, Wales, UK.
[2]Department of Earth Sciences, University of Oxford, South Parks Road, Oxford, OX1 3AN, England, UK.
[3]Department of Earth and Environmental Sciences, University of Michigan, 1100 North University Avenue, Ann Arbor, 40819, MI, USA.
[4]School of Earth Sciences, University of Bristol, Queens Road, Bristol, BS8 1RJ, England, UK.

*Corresponding author(s). E-mail(s): pantonjc@cardiff.ac.uk;

Content

- Supplementary Figures S1–S13

Supplementary Figures

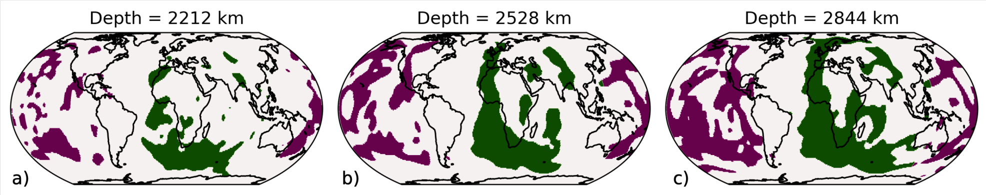

Fig. S1 Depth sections at 2212 km (a), 2528 km (b) and 2844 (km) of the areas identified as S-LLVPs in the Pacific (purple) and African (green) regions for simulation RCY.

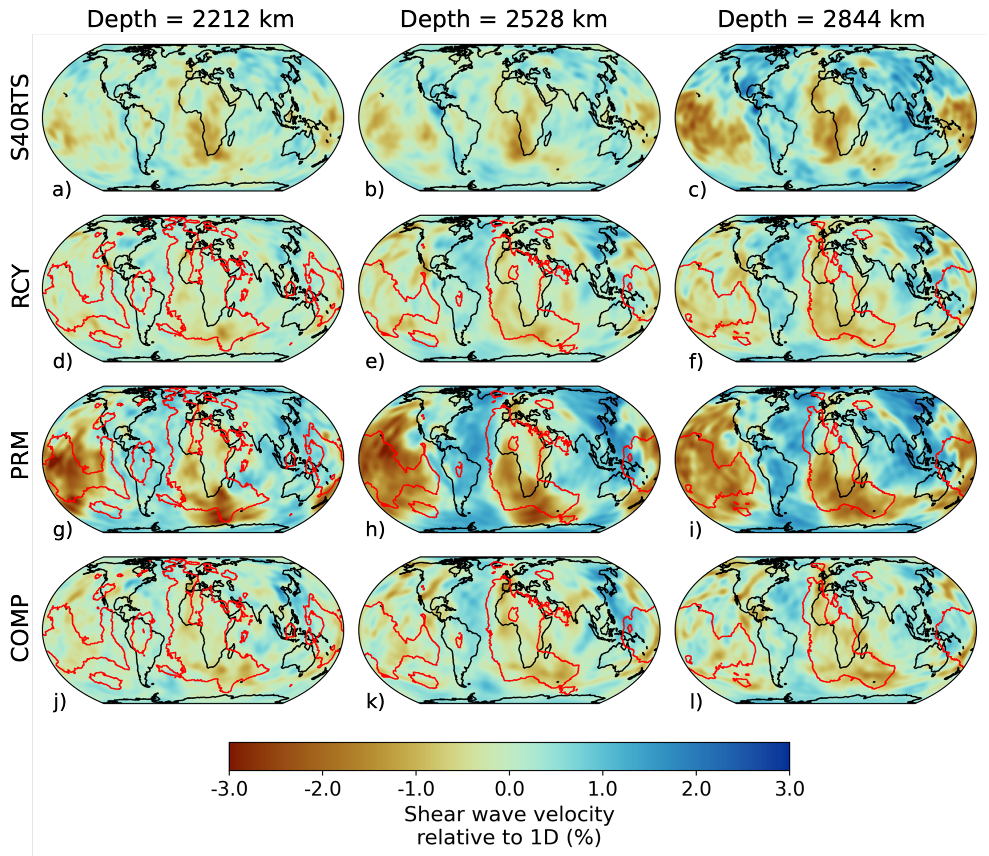

Fig. S2 Mantle structure at 2212 km (left column), 2528 km (centre column), and 2844 km (right column) depth, showing δV_s according to seismic tomography model S40RTS (a-c, top row), as predicted in simulation RCY (d-f), as predicted in simulation PRM (g-i) and as predicted in simulation COMP (j-l), all filtered by the S40RTS resolution. Red outlines are derived from a vote map of low velocity regions detected in 18 shear wave tomography models [1], and indicate where at least 5 models are in agreement.

References

[1] Hosseini, K., Matthews, K.J., Sigloch, K., Shephard, G.E., Domeier, M., Tsekhmistrenko, M.: SubMachine: Web-Based Tools for Exploring Seismic Tomography and Other Models of Earth's Deep Interior. Geochemistry, Geophysics, Geosystems **19**(5), 1464–1483 (2018) https://doi.org/10.1029/2018GC007431 . _eprint: https://onlinelibrary.wiley.com/doi/pdf/10.1029/2018GC007431. Accessed 2023-07-07

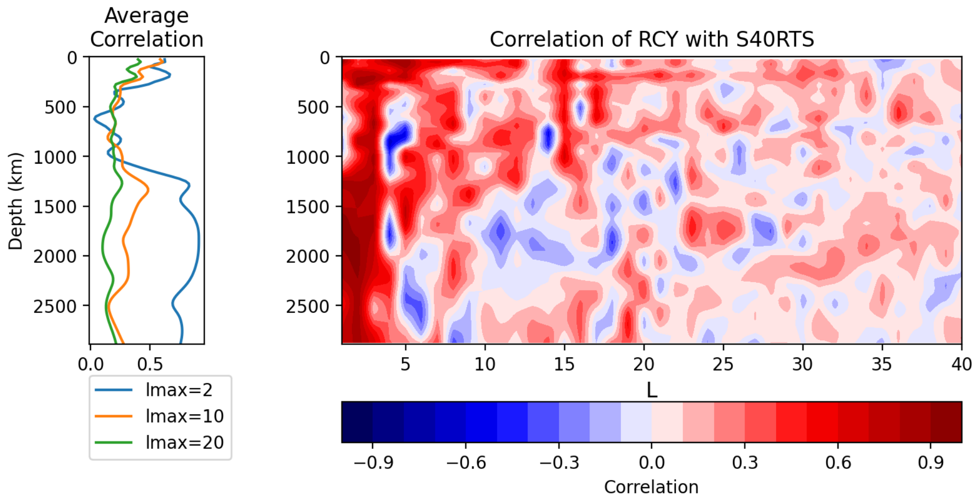

Fig. S3 Correlation between simulation RCY and S40RTS over depth and spherical harmonic degree, L, up to $L = 40$ (right panel) and average correlation with depth up to spherical harmonic degrees 2, 10 and 20 (left panel).

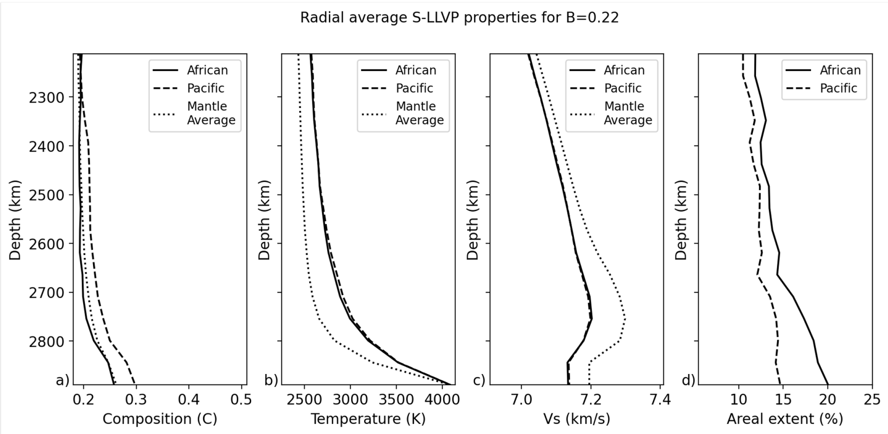

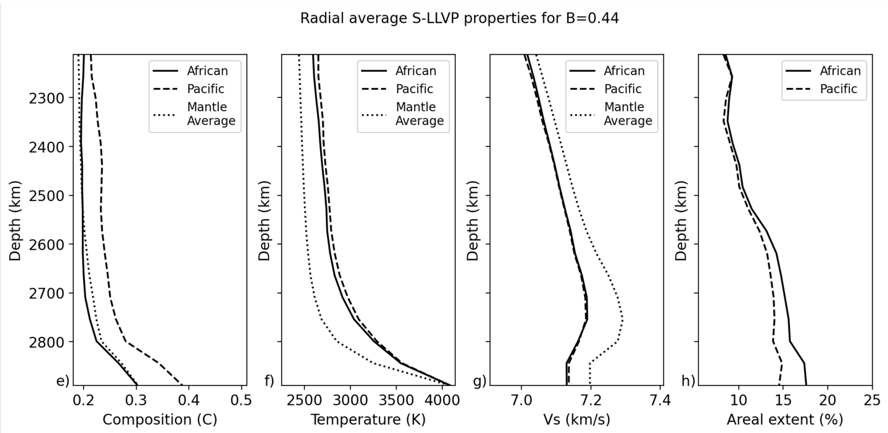

Fig. S4 Radial profiles of (a,e) bulk composition, (b,f) temperature, (c,g) V_s, and (d,h) areal extent at each radial layer for the African (solid line) and Pacific (dashed line) S-LLVPs identified in simulations (a-d) B=0.22 and (e-h) B=0.44.

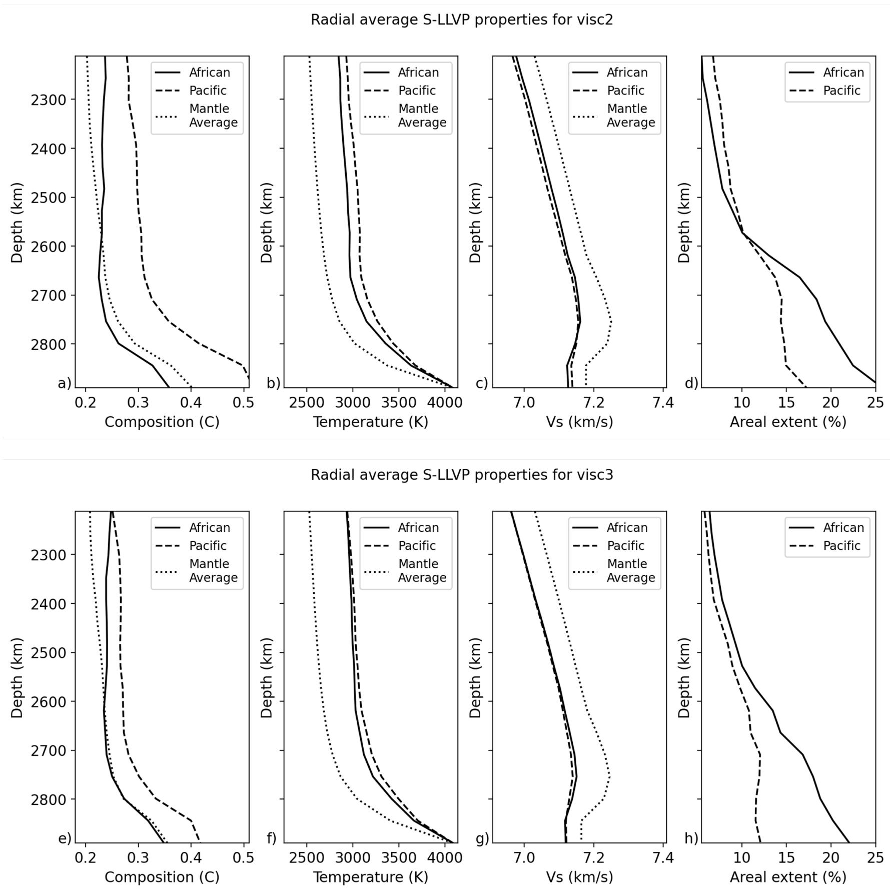

Fig. S5 Radial profiles of (a,e) bulk composition, (b,f) temperature, (c,g) V_s, and (d,h) areal extent at each radial layer for the African (solid line) and Pacific (dashed line) S-LLVPs identified in simulations (a-d) visc2 and (e-h) visc3.

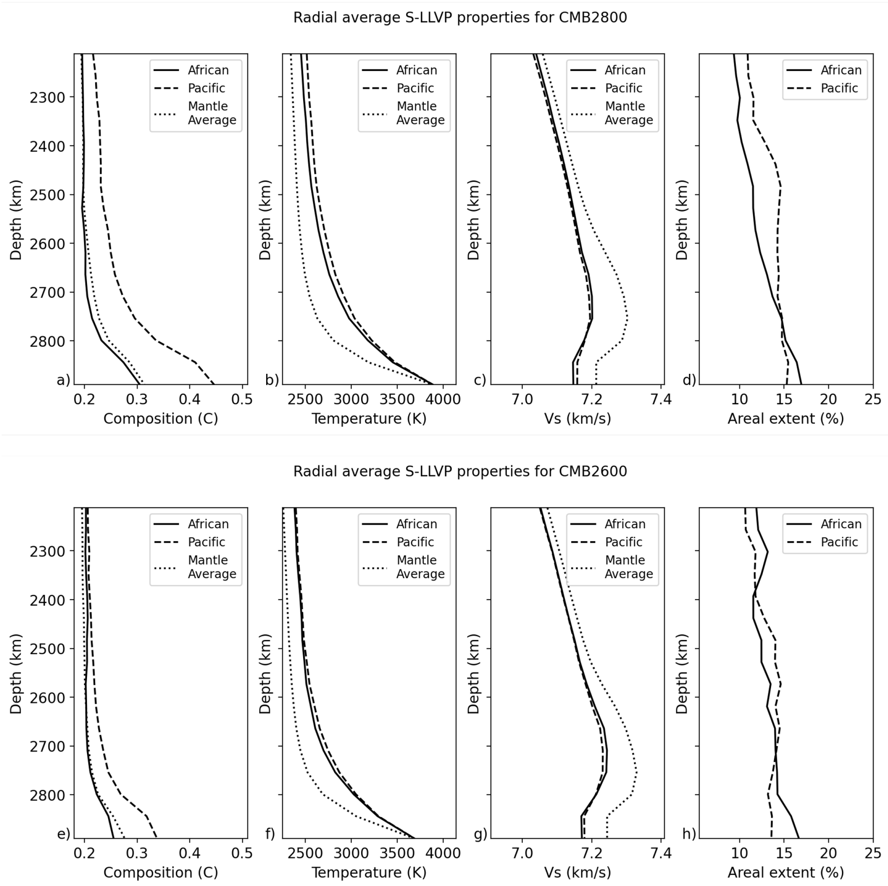

Fig. S6 Radial profiles of (a,e) bulk composition, (b,f) temperature, (c,g) V_s, and (d,h) areal extent at each radial layer for the African (solid line) and Pacific (dashed line) S-LLVPs identified in simulations (a-d) CMB2800 and (e-h) CMB2600.

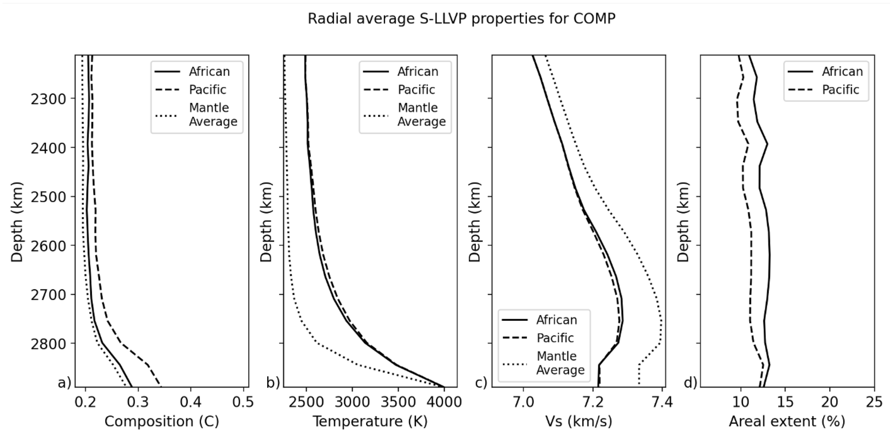

Fig. S7 Radial profiles of (a) bulk composition, (b) temperature, (c) V_s, and (d) areal extent at each radial layer for the African (solid line) and Pacific (dashed line) S-LLVPs identified in simulation COMP.

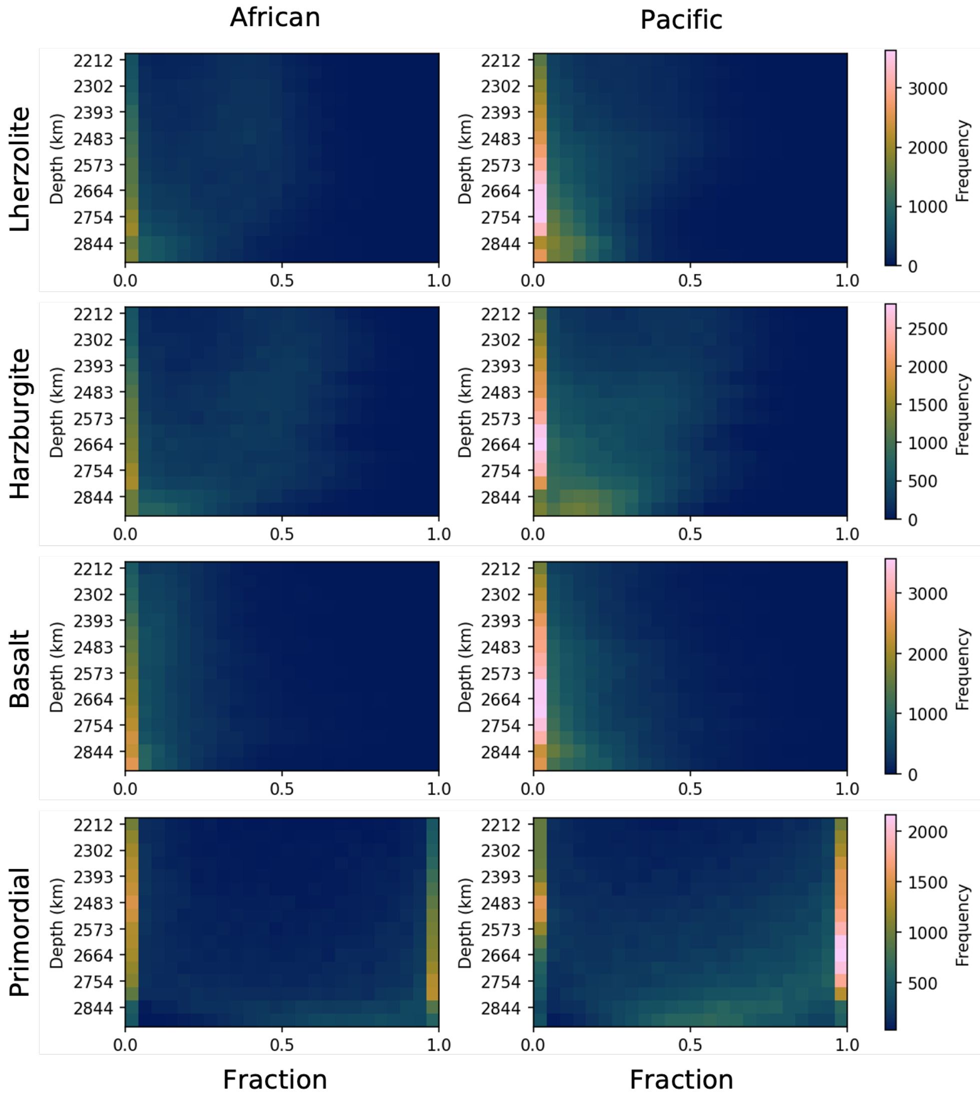

Fig. S8 2D histograms for proportion of different characteristic lithologies in the African (left column) and Pacific (right column) S-LLVPs in model PRM at each radial layer of the dynamic simulation between 2212 km and 2890 km depth. The four characteristic lithologies are (a) harzburgite, (b) lherzolite, (c) basalt, and (d) the primordial component .

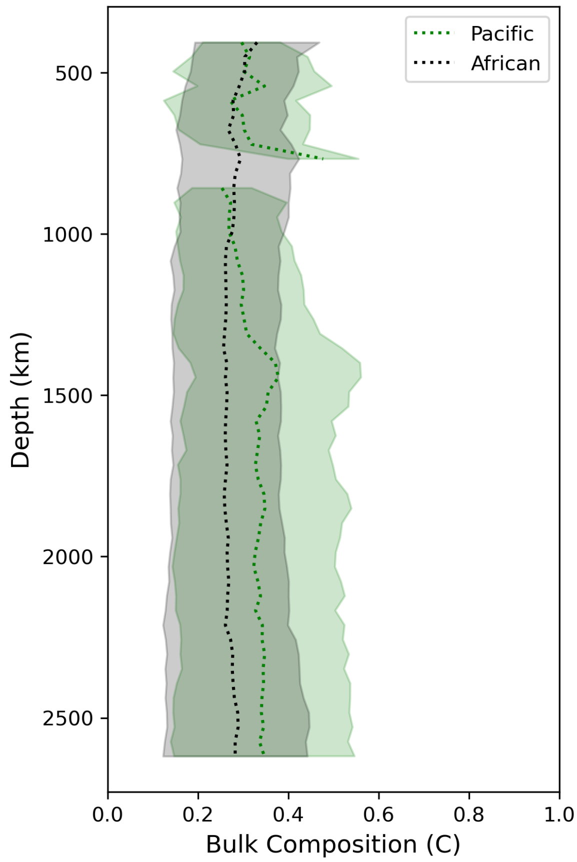

Fig. S9 Radial mean bulk composition of plumes associated with the Pacific and African S-LLVPs (solid lines) with ± 1 standard deviation shown with shaded area.

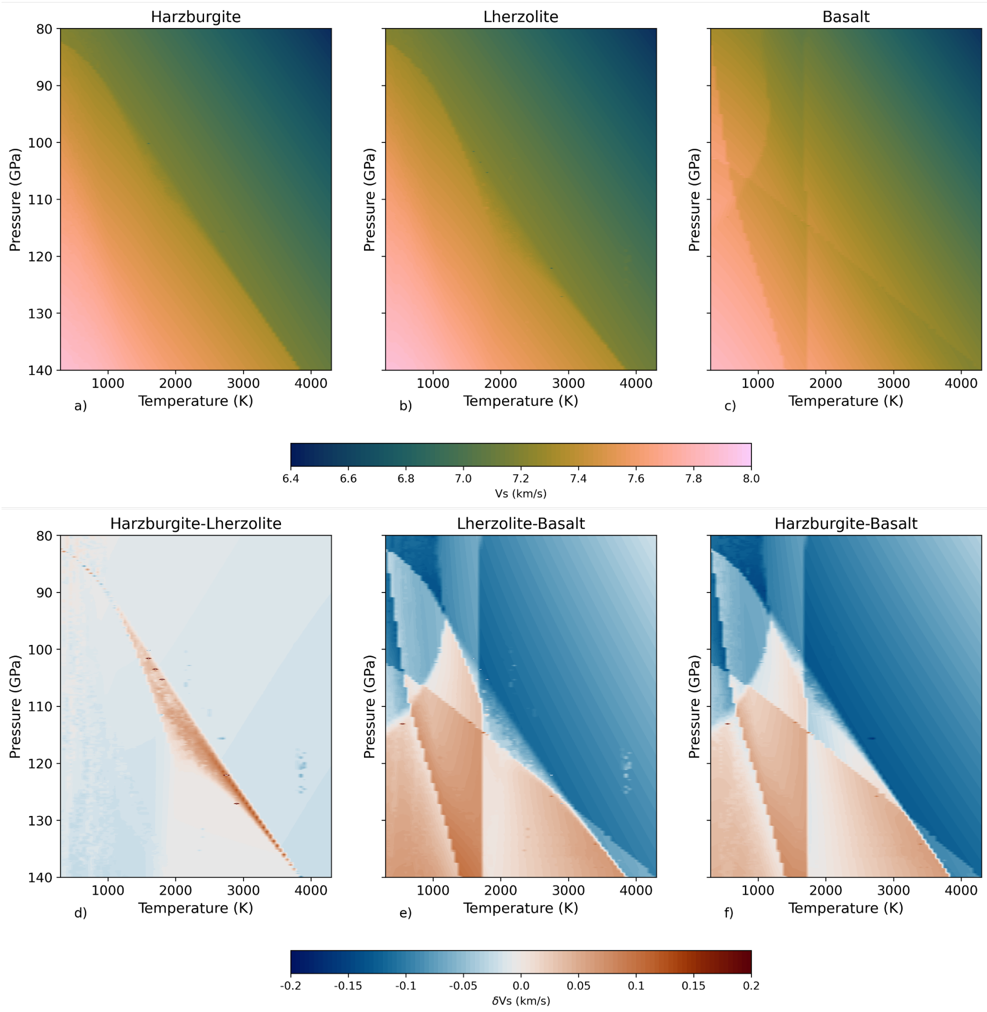

Fig. S10 Mineral physics estimates of V_s in temperature and pressure space. The top show shows V_s for the characteristic lithologies of (a) harzburgite, (b) lherzolite, and (c) basalt. The bottom row shows the differences in V_s between (d) harzburgite and lherzolite, (e) lherzolite and basalt, and (f) harzburgite and basalt. See Methods **??** for full details of how the tables were produced.

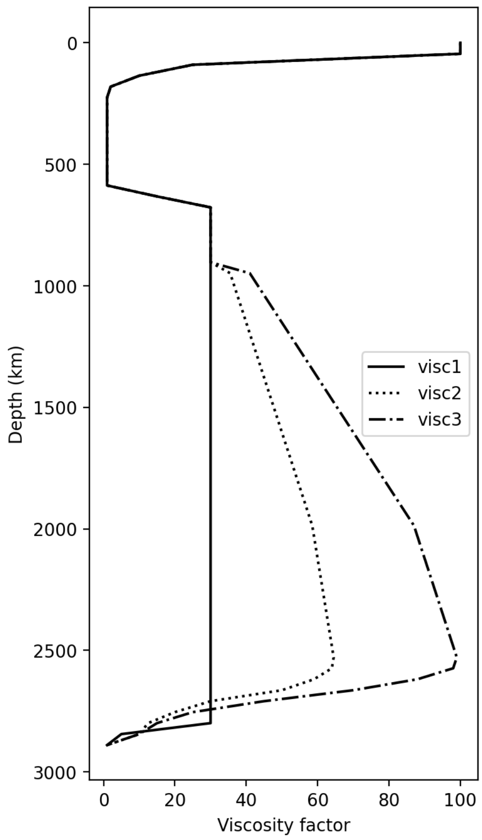

Fig. S11 Radial profile of the viscosity scaling factors used in the simulations listed in Table **??**.

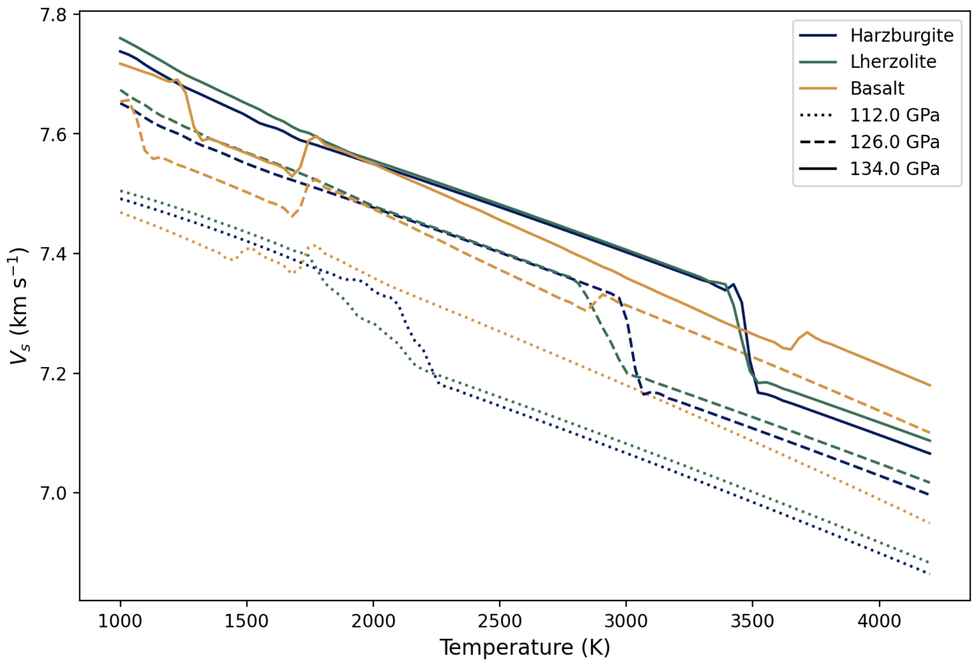

Fig. S12 Variation of predicted V_s with temperature at constant pressure, shown for several characteristic lithologies: Harzburgite (blue), lherzolite (green) and basalt (gold). Different lines indicate velocities at different pressures: 134 GPa (solid line), 126 GPa (dashed line) and 112 GPa (dotted line).

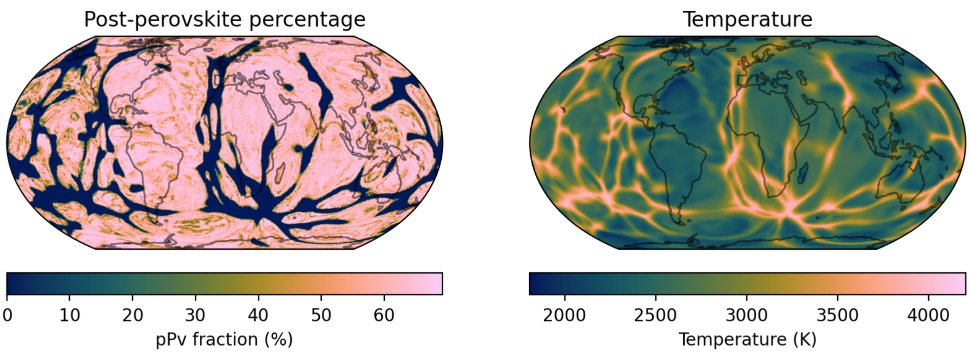

Fig. S13 Predicted distribution of post-perovskite in simulation RCY, shown at a depth of 2755 km. Left panel indicates the fraction of post-perovskite at this depth, the right panel shows the temperature field with a synthetic adiabat added.